Materials Advances

PAPER

Check for updates

Synthesis and characterization of safranal@ MIL-88B(Fe) nanostructures and their preliminary anticancer and antibacterial characteristics†

Alia Alkaabi, [ID] [ab] Khansa Ahsan, [ID] [a] Nayla Munawar, [ID] [a] Abdelouahid Samadi, [ID] [a] Hesham El-Maghraby, [ID] [a] Amr Amin [ID] [c] and Yaser Greish [ID] *[a]

Applications of metal–organic framework (MOF) nanostructures in biomedicine have rapidly expanded over the past decade. MOFs are characterized by their high functionality, surface area, and porosity, providing an ideal platform for several biomedical applications. This study explores the potential of a novel therapeutic approach for liver cancer, incorporating Safranal, a bioactive molecule derived from saffron, within the iron-based metal–organic framework (MOF), MIL-88B(Fe). The successfully loaded Safranal-MIL-88B(Fe) composite nanostructure was comprehensively characterized and tested for its effectiveness against HepG2 liver cancer cells. Furthermore, we investigated its antibacterial efficacy against *Escherichia coli* (*E. coli*) and *Lactobacillus* strains. The proposed mechanism of action of the Safranal-MIL-88B(Fe) nanostructures potentially shows the effect of the release of the ferric ions and Safranal *in vitro* against HepG2 cancer cells and both bacterial strains. Our findings show significant promise for Safranal-loaded MIL-88B(Fe) as a dual-purpose therapeutic agent, opening exciting avenues for future biomedical applications.

Introduction

Emerging nanomaterials have recently created a paradigm change in biomedical research, offering innovative drug delivery methods and diagnostic tools. Metal–organic frameworks (MOFs) have attracted scientific attention due to their numerous functions in various sectors, including gas storage and separation, catalysis, water harvesting, sensors, electronics, and, most importantly, biomedical applications.[1,2] The unique properties engineered into MOF nanoparticles hold particular promise for medical advancements. MOFs offer several advantages, including exceptional loading capacity, tunable biodegradability, and reproducible synthesis protocols. Moreover, unlike conventional drug delivery systems, MOFs possess the unique ability to create a carrier scaffold with inherent theranostic capabilities, providing both therapeutic and diagnostic functionalities.[3]

MOFs are porous crystalline materials with coordinating organic ligands and inorganic metal ions (or clusters).[4,5] Their

intrinsic features, including well-ordered and controllable porosity, remarkable crystallinity, and large surface areas, make them suitable host matrices for immobilizing biomolecules. The Materials of Institute Lavoisier (MIL) series exemplifies these MOF nanostructures, renowned for their remarkable framework flexibility. The unit cells of a number of these MIL nanostructures, such as MIL-88A and MIL-88B, can reversibly swell and shrink without compromising the overall framework topology, a phenomenon known as breathing behavior.[6,7] This unique property allows the carrier to adapt its pore size intelligently to accommodate various drugs, subsequently stabilizing sensitive molecules.[8]

Iron-containing MOFs (Fe-MOFs) have attracted much interest due to their superior safety and biodegradability profiles.[9–11] Most Fe-MOFs are members of well-known MIL and BioMOF families, including MIL-53, MIL-88A, MIL-88B, MIL-100, MIL-101, MIL-127, BioMOF-1, and BioMOF-5.[12–20] These MOFs have shown great potential as drug carriers, successfully encapsulating and delivering various therapeutic drugs, including busulfan, azidothymidine triphosphate, cidofovir, and doxorubicin.[21]

Addressing concerns regarding the potential toxicity of metals employed in MOFs, a study has explored a series of fourteen MOFs with varying compositions (Fe, Zn, and Zr; carboxylates or imidazolates). This investigation revealed iron (Fe) as the least toxic metal among those tested.[22] Consequently, developing Fe-MOFs with iron as the core metal ion has garnered significant interest due to their unique properties and potential applications.

a Department of Chemistry, Al Ain, United Arab Emirates.
E-mail: y.afifi@uaeu.ac.ae
b Department of Biology, United Arab Emirates University, Al Ain, United Arab Emirates
c Department of Basic Medical Sciences, College of Medicine, Sharjah University, Sharjah, United Arab Emirates
† Electronic supplementary information (ESI) available. See DOI: https://doi.org/10.1039/d4ma00345d

The incorporation of iron introduces a range of additional functionalities, including redox activity, intrinsic peroxidase-like activity, diverse catalytic properties, and even antimicrobial and antifungal properties.[23–26]

Fe-MOFs also hold significant promise for cancer treatment by inducing ferroptosis in cancer cells, a regulated cell death characterized by iron-dependent lipid peroxidation. These MOFs can trigger ferroptosis through various mechanisms. Firstly, the iron within Fe-MOFs facilitates the Fenton effect, generating highly reactive hydroxyl radicals ($\bullet OH$) from hydrogen peroxide (H_2O_2), leading to oxidative stress and cell death.[27] Additionally, Fe-MOFs contribute to producing reactive oxygen species (ROS) within the cancer cells, further disrupting cellular homeostasis and promoting cell death.[28–30] Moreover, the iron centers in Fe-MOFs can form coordination bonds with specific anticancer drugs, enhancing targeted drug delivery and controlled release and ultimately improving chemotherapy efficacy.[27] These diverse mechanisms highlight Fe-MOFs' potential as a powerful tool in cancer therapy.

A study on MIL-88B-type multivariate (MTV-1) nanocarriers serves as an example. These nanocarriers, made of a mixed linker and metals (iron and cobalt), contained 5-fluorouracil (5-FU) and curcumin (CUR). MTV-1@5-FU + CUR demonstrated pH-responsive drug release, with more drugs released at pH 5.5 (cancer microenvironment). MTV-1 MOFs also showed peroxidase-like activity and catalyzed H_2O_2 breakdown in chemodynamic treatment. Cell assays revealed a substantial inhibitory impact against HepG2 cells (IC_{50} = 78.7 μg mL^{-1}). This demonstrates Fe-MOFs' potential in combination therapy, as dual-drug loading, pH-responsive release, and chemodynamic therapy hold promise for multifunctional anticancer treatment.[31]

Safranal, derived from saffron, has been of interest due to its potential pharmacological effects on liver cancer. Safranal demonstrated promising outcomes in decreasing HepG2 cell viability, with an IC_{50} of 500 μM after 48 hours, highlighting its potential as a liver cancer therapy. Additionally, Safranal induced morphological changes in HepG2 cells, such as rounded shapes, shrinkage, and increased detachment, supporting its cytotoxic effects. Also, Safranal suppressed colony formation in HepG2 cells in a dose-dependent manner, with the most effective concentration at 100 μM.[32] Furthermore, Safranal showed pro-apoptotic effects in HepG2 cells, activating intrinsic and extrinsic caspases and promoting cell death through endoplasmic reticulum (ER) stress.[32] It reduced HUVEC growth (IC_{50} = 300 μM) and blocked VEGF release in HepG2 cells, indicating potential anti-angiogenic effects.[33] Furthermore, Safranal prevented endothelial cell migration and tube formation, supporting its anti-angiogenic properties.[33] These findings highlight Safranal's various effects on liver cancer cells and its potential as a valuable therapeutic agent. However, stability and bioavailability limitations still hinder the clinical use of Safranal. It has been revealed that Safranal concentrations in mouse and rat plasma decrease significantly over time, highlighting this challenge.[34] This study aims to investigate the intrinsic anticancer potential of MIL-88B(Fe) in combination with Safranal while considering the constraints of Safranal's stability and bioavailability.

Bacterial infections, on the other hand, remain among the leading causes of morbidity and mortality, posing a significant global public health risk. Antibiotic overuse contributes to the spread of antimicrobial resistance. The emergence and spread of antimicrobial resistance (AMR) results in the development of multidrug-resistant (MDR) bacteria, escalating global public health concerns.[35] Nanoparticles (NPs) are usually used in antibiotic delivery systems, bacterial detection systems for microbial diagnostics, and antibacterial vaccines to control bacterial infections. While the precise mechanisms of NPs' antibacterial action are unknown, established possibilities include promoting oxidative stress, metal ion release, and non-oxidative routes.[36] In the past few years, MOFs have gained significant attention for diverse antibacterial applications due to their antibacterial capabilities resulting from different physical and chemical features. These include metal ion or organic compound controlled release and enzyme-like, photocatalytic, and photothermal activity.[37]

This work aims to overcome Safranal's limitations by incorporating it into/onto the MIL-88B(Fe) structure, paving the way for natural products to emerge as effective medicines in the treatment of liver cancer. The study also investigates MIL-88B(Fe)'s promising antibacterial characteristics and potential as a dual-purpose therapeutic agent for cancer and bacterial infections. This research adds to the growing understanding of using Fe-MOFs in biomedicine. It demonstrates the potential of safranal-loaded MIL-88B(Fe) as a diverse and practical treatment approach.

Experimental procedures

Materials

The following chemicals and reagents were used in this study for the preparation of MIL-88B(Fe) and the SAF@MIL-88B(Fe) nanostructures: iron(III) chloride hexahydrate (FeCl$_3$.6H$_2$O), terephthalic acid (H$_2$BDC), dimethylformamide (DMF), ethanol, and safranal were all obtained as analytical-grade chemicals from Sigma-Aldrich and were used as received.

For the evaluation of the anticancer characteristics of the MIL-88B(Fe) and the SAF@MIL-88B(Fe) nanostructures, the following chemicals and reagents were used: antibiotic–antimycotic solution for cell culture – A5955, fetal bovine serum (10%), 3-[4,5-dimethylthiazol-2-yl]-2,5-diphenyltetrazolium bromide (MTT), dimethyl sulfoxide (DMSO), and Dulbecco's phosphate buffered saline – Lot No. RNBL0732 were all obtained from Sigma-Aldrich. A HepG2 human liver carcinoma cells strain was obtained from ATCC (HB-8065), the cell culture media (RPMI 1640 Medium, with L-Glutamine) was obtained from Capricorn Scientific GmbH, Germany, a 0.25% trypsin solution was obtained from Cytiva, Marlborough, MA, USA, and a Mounting Medium containing 4',6-diamidino-2-phenylindole (DAPI) (ab104139) was obtained from Abcam. In addition, a 4% paraformaldehyde was prepared in our laboratories.

For the evaluation of the antibacterial characteristics of the MIL-88B(Fe) and the SAF@MIL-88B(Fe) nanostructures, the following chemicals and reagents were used: *E. coli* strain

obtained from the American Type Culture Collection (ATCC), *Lactobacillus* strain isolated from probiotic yogurt, LB Agar and LB Broth obtained from Lab M Limited, UK, Agarose obtained from Sigma-Aldrich, Bacterial Genomic DNA Isolation Kit (ab288102) obtained from Abcam, UK, RedSafe™ Nucleic Acid Staining Solution (20 000×) obtained from iNtRON Biotechnology, South Korea, 1kb DNA Ladder obtained from Promega, and Gel Loading Dye Purple (6×) obtained from New England BioLabs.

Methods

Synthesis of MIL-88B(Fe). MIL-88B(Fe) was prepared using a facile solvothermal procedure. In a typical experiment, a solution containing a 1:1 molar ratio of the same reactants mentioned above ($FeCl_3 \cdot 6H_2O$ and H_2BDC) was prepared in dimethylformamide (DMF). The mixture was then transferred to a Teflon tube and subjected to a pre-heated oven at 150 °C for 3 hours. Subsequently, the resulting MIL-88B(Fe) crystals underwent washing steps using DMF and ethanol. Furthermore, the washed crystals were dried overnight at room temperature, followed by drying in a vacuum oven at 80 °C for 24 hours to remove any remaining moisture. The detailed synthesis procedure is illustrated in Scheme 1.

Preparation of SAF@ MIL-88B drug delivery system. Due to Safranal's insolubility in aqueous media, a series of EtOH solutions with safranal concentrations of 3%, 5%, 7%, and 10%, amounting for 1.8, 3.0, 4.2, and 6.0 mg mL^{-1}, respectively of Safranal, were prepared. MIL-88B(Fe) was stirred in the Safranal–EtOH solution for 12 hours. The resulting MIL-88B(Fe) precipitate was isolated, underwent overnight drying at room temperature, followed by an additional drying step in a vacuum oven at 25 °C for 24 hours. The aliquots of all solutions were analysed for the remaining Safranal using UV-vis technique. Scheme 1 visually represents the synthesis, loading, and drying steps of SAF@MIL-88B(Fe).

Structural and morphological characterization. Fully dried powder samples of MIL-88B(Fe) and SAF@MIL-88B(Fe) containing different proportions of Safranal were characterized for their structure and morphology before and after exposure to PBS and RPMI media. XRD data were collected on a Rigaku MiniFlex 600-C powder XRD diffractometer equipped with Fe-Kα radiation (λ = 1.542 Å). Diffraction data were obtained in the 2θ angle range of 20–70 degrees using a Bruker D8 Advance Diffractometer. Fourier transform infrared (FTIR) spectra (4000–400 cm^{-1}) were obtained from KBr pellets using a Bruker Vector 22 instrument. The thermostability of the material was investigated through thermogravimetric analysis (TGA) using a Shimadzu DTG60 thermogravimetric analyzer. The analysis involved a temperature ramp of 10 °C min^{-1} in a nitrogen atmosphere. The morphology and particle size of the MOF samples were assessed through scanning electron microscopy (SEM) using a Thermoscientific Quattro S SEM instrument. The samples' surface areas and total pore volumes were determined from N_2 adsorption isotherms at 77 K using a Quantachrome Autosorb-1 volumetric gas sorption instrument. Before analysis, the MOF materials underwent degassing at 150 °C for 48 hours to eliminate all solvents and moisture from the pores.

To confirm the presence of Safranal in the MOF network, a solution of 0.7 mL dimethyl sulfoxide-d_6 was added to 5 mg of MOF material. The resulting solution was heated until the powder completely dissolved. ^1H NMR spectra were recorded at 25 °C in DMSO-d_6 using a Varian-400 MHz instrument (USA), with solvent peaks at 2.50 ppm as internal references. The assignment of chemical shifts was relative to a known standard Safranal.
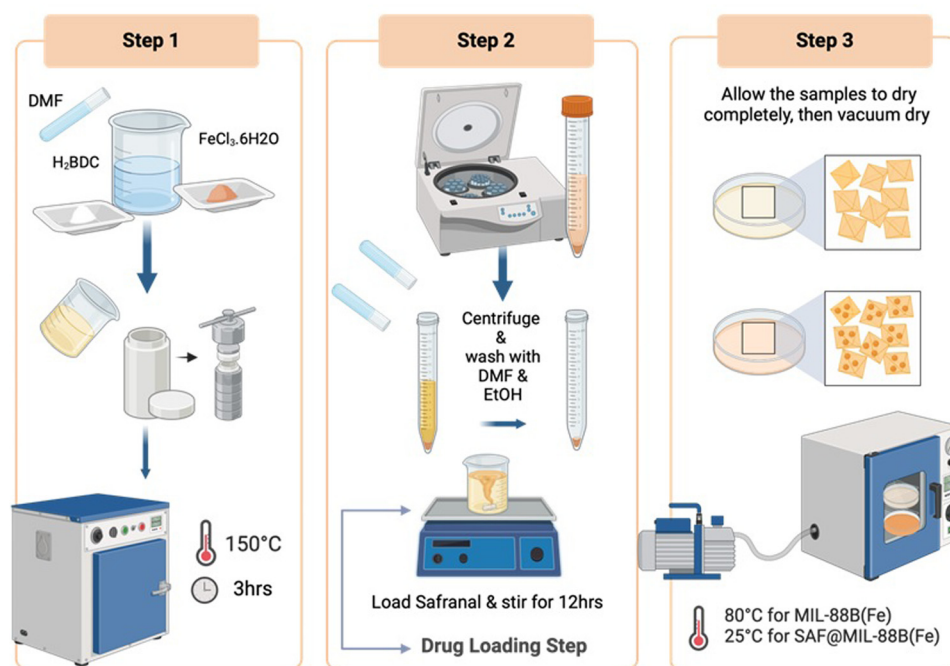
Scheme 1   Procedure of fabrication of MIL-88B(Fe) and SAF@MIL-88B(Fe) nanostructures.

The release of Fe^{3+} ions and Safranal from the pure and Safranal-loaded MIL-88B(Fe) nanostructures was monitored using ICP-MS and UV-VIS techniques, respectively. An inductively coupled plasma-mass spectroscopy (PERKIN ELMER ICP-MS, NEXION-2000G), USA used was for the follow up of release of Fe^{3+} ions. The release of Safranal was monitored using a UV-visible spectrophotometer. Fig. S1a (ESI†) shows a series of absorption spectra collected for different concentrations of safranal, where two main peaks were noticed at λ_{max} values of 205 and 320 nm. A calibration curve was made for the peak at 205 nm, as shown in Fig. S1b (ESI†).

SAF@MIL-88B release studies. Both MIL-88B(Fe) and SAF@MIL-88B(Fe) containing 7 wt% Safranal were evaluated for their stability in PBS solution at pH 7.4. Both types of nanoparticles were studied for the release of Fe^{3+} ions with time, while the SAF@MIL-88B(Fe) composite nanoparticles were monitored for the release of Safranal with time at pH 7.4.

A 100 mL PBS solution containing MOF powder (at a concentration of 3 mg mL^{-1}) was prepared in a conventional experimental setting. All samples were placed in a shaker incubator set at 100 rpm and 37 °C for up to 72 hours. Solution aliquots were collected at intervals of 0.5, 1, 6, 24, and 72 hours. To keep the volume consistent, fresh PBS was added after each 10 mL aliquot was removed. The collected solutions were filtered through a 0.2 μm syringe filter into separate vials and analyzed for [Fe^{3+}] composition using the inductively coupled plasma-atomic emission spectroscopy (ICP-AES) technique. The experiment was repeated three times to ensure the reliability of the results.

To assess drug (Safranal) release, a 100 mL PBS solution containing SAF@MIL-88B(Fe) at a concentration of 3 mg mL^{-1} (inclusive of MIL-88B(Fe) + 7% Safranal) sample was prepared in a conventional experimental setting. All samples were placed in a shaker incubator set at 100 rpm and 37 °C for up to 144 hours. Solution aliquots were collected at intervals of 0.5, 1, 3, 6, 24, 48, 72, 96, 120, and 144 hours. After withdrawing 10 mL aliquots, fresh PBS was added each time an aliquot was removed to ensure a constant volume. The collected solutions were filtered through a 0.2 μm syringe filter into separate vials and analyzed using a UV-vis spectrophotometer. The experiment was repeated three times to ensure the reliability of the results.

HepG2 cell growth. HepG2 human liver carcinoma cells (ATCC, HB-8065) were obtained and maintained in RPMI 1640 medium (Capricorn Scientific GmbH, Germany), supplemented with 10% fetal bovine serum (Sigma Aldrich, St. Louis, MO, USA), 1% penicillin (100 U mL^{-1}), and 100 μg mL^{-1} streptomycin (Sigma Aldrich, St. Louis, MO, USA). The cells were cultured at 37 °C with 5% CO_2 and sub-cultured every 3–5 days using 0.25% trypsin (Cytiva, Marlborough, MA, USA).

MTT assay. HepG2 cells were seeded at a density of 7000 cells per well in 96-well plates, each containing 100 μL of complete growth medium. Following cell attachment, various concentrations of the MOF – 2.5, 5, 10, 25, 50, 75, and 100 μg mL^{-1} – were administered for 24 and 48 hours. A stock solution of the MOF material at 1 mg mL^{-1} concentration was prepared in a culture medium. The initial stock solution was diluted using the cell culture medium to prepare working concentrations. The suspension of the compound was freshly prepared on the day of treatment. Subsequently, the cells underwent treatment with 3-[4,5-dimethylthiazol-2-yl]-2,5-diphenyltetrazolium bromide (MTT) (Sigma Aldrich) and were incubated for 3 hours. To avoid potential absorbance interference from the MOF material, treated wells were carefully washed with RPMI media and 1X PBS, and fresh media was added before the addition of the MTT reagent. Formed formazan crystals were dissolved using dimethyl sulfoxide (DMSO), and the resulting product's absorbance was measured at 570 nm using the GloMax Microplate Reader (Promega). The experiment was conducted in triplicate to ensure the reliability of the results. The cell viability, expressed as a percentage of the untreated control, was calculated as follows: Percent of viable cells = (Absorbance of treated cells/Absorbance of control cells) × 100. Statistical significance was denoted by *$P \leq 0.05$, **$P \leq 0.01$, ***$P \leq 0.001$, and ****$P \leq 0.0001$

DAPI fluorescence staining. HepG2 cells were seeded at a density of 7000 cells per well in 96-well plates and allowed to incubate overnight. Subsequently, the cells were treated with varying concentrations of MIL-88B(Fe) and SAF@MIL-88B(Fe) (2.5, 5, 10, and 25 μg mL^{-1}) for 24 hours. Following treatment, the culture supernatant was removed, wells were washed with cold PBS, then fixed using 4% paraformaldehyde (50 μL) for 10 minutes at room temperature. The fixed cells were then incubated with one drop of mounting medium containing 4′,6-diamidino-2-phenylindole (DAPI) (ab104139) in the dark for 1 hour at room temperature. The morphology was assessed using an IX53 microscope (Olympus).

Antibacterial zone of inhibition assay. The antibacterial activity of MIL-88B(Fe) and SAF@MIL-88B(Fe) against *E. coli* BL21 (DE3) (Gram-negative) and *Lactobacillus* (Gram-positive) cells was determined using ASTM E2149-13a approach with slight modifications as described below. On LB agar plates, *E. coli* and *Lactobacillus* inocula were spread, and 0.07 g MOF disks were placed in the center, with terephthalic acid disks serving as controls. After a 16-hour incubation at 37 °C, the diameter of the non-growth zone around each MOF disk was measured, indicating the zone of inhibition of microbial growth. The link between the MOF and the corresponding inhibition zone is plotted graphically, revealing information about the MOF's antimicrobial action over the chosen period.

Antibacterial minimum inhibitory concentration (MIC) assay. The microtiter broth dilution method was used to determine the minimum inhibitory concentration (MIC) for MIL-88B(Fe) and SAF@MIL-88B(Fe), targeting the growth inhibition of *E. coli* and *Lactobacillus* microorganisms. Bacterial suspensions with a final concentration of 1×10^5 CFU mL^{-1} were prepared in 5 mL LB broth, and 5 μL of each suspension was added to individual wells in a 96-well plate. The MOFs were serially diluted twofold in concentrations ranging from 7.81 μg to 2 mg. The plates were incubated at 37 °C overnight for antibacterial assessment, and a negative control lacking MOF powder was included. The experiment was scaled up to a final volume of 5 mL in test tubes to avoid cross-contamination.

Agarose gel electrophoresis for DNA disintegration analysis. DNA degradation and disintegration were examined using agarose gel electrophoresis to evaluate cell death caused by MIL-88B(Fe) and SAF@MIL-88B(Fe). *E. coli* and *Lactobacillus* were exposed to varied Fe-MOF concentrations (ranging from 0 to 1.5× MIC) and incubated at 37 °C overnight. After incubation, each sample was collected and centrifuged, and the DNA was extracted using the Bacterial Genomic DNA Isolation Kit (ab288102). The NanoDrop 2000 from Thermofisher was used for DNA quantification. Subsequently, 5 µL of the treated Fe-MOFs samples were combined with 1.5 µL of loading dye and subjected to agarose gel electrophoresis for qualification analysis of treated and non-treated samples.

Results and discussion

Characterization of MIL-88B(Fe) and SAF@MIL-88B(Fe) nanostructures

The as-prepared MIL-88B(Fe) was characterized for its structure and morphology to confirm its phase purity. Fig. 1(a) shows the XRD pattern of the as-prepared MIL-88B(Fe), showing its high crystallinity, compared with the simulated XRD pattern of the same phase.[38] The most intense peak, representing the 101 plane, was observed at 2θ: peaks at 9.44°. Other peaks at 10.62, 12.62, 18.9, and 22.00° representing the 002, 102, 202 and 211 planes were also observed, as shown in Fig. 1(a). The absence of a peak below 2θ: 7.00° could be related to the synthesis procedure which was carried out in the presence of DMF solvent, which was previously shown to alter the crystal structure of the MIL-88B(Fe) without affecting its purity.[39] These peaks confirm the phase purity of the as-prepared MIL-88B(Fe) nanostructure.[39] The slight shifts in the peak positions and intensities, as compared with the simulated pattern, could be related to the partial variation in the crystal growth of the precipitated MIL-88B(Fe) crystallites. Considering the low BET surface area of the as-prepared MIL-88B(Fe), as will be discussed later, it could be implied that this is the close form of the structure.

Fig. 1(b) shows the FT-IR spectrum of the as-prepared MIL-88B(Fe). Three main features could be observed: bands at 1659.1, 1595.9, 1503.2, 1436.9, and 1390.3 cm^{-1} are attributed to the $-O{=}C-O^{-}$ group, and bands at 748.5 and 1014.4 cm^{-1} are attributed to the C–H group of the terephthalate linker.[36] The Fe–O absorption is shown at 554.9 cm^{-1}, while the broad bands at 3423.1 cm^{-1} are related to the physically adsorbed water molecules.[40] Fig. 1(c) shows the TGA-DTG thermograms of the MIL-88B(Fe) nanostructure. The TGA thermogram starts with a slow rate of weight loss until 340 °C, which is attributed to the removal of weakly adsorbed volatile compounds, including water and/or organic solvents. This is followed by two thermal events, which were also confirmed by the DTG thermogram at 366.2 and 469.3 °C. These events amount to a weight loss of 35 and 71%, respectively. These events are related to the breakdown of the MOF structure at 366.2 °C, followed by a complete decomposition of the organic content of the MOF at 469.3 °C. An iron oxide residue is formed after 600 °C after complete decomposition of the MOF structure.

Fig. 1(d) shows the morphology of the as-prepared MIL-88B(Fe) nanostructures. A homogeneous particle size distribution of the
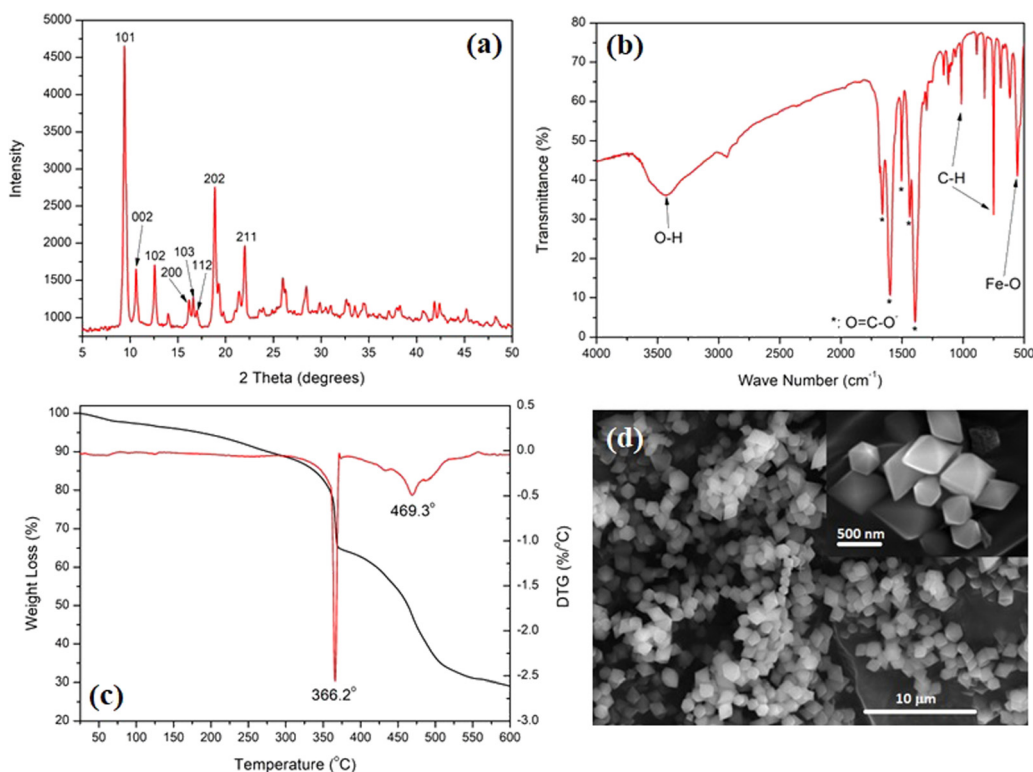

Fig. 1 XRD pattern (a), FT-IR spectrum (b), TGA-DTG thermograms (c), and SEM micrographs (d) of the as-prepared MIL-88B(Fe) nanocrystals.

MIL-88B(Fe) diamond-shaped crystals can be observed. The inset of the SEM micrograph shows a sharp-edged diamond-shaped MIL-88B(Fe) crystal with an average length of 600 nm and width of 500 nm. These findings confirm the phase purity and morphology of the synthesized MIL-88B(Fe) nanocrystals. Fig. S2 (ESI†) shows the N_2-adsorption–desorption hysteresis of the as-prepared MIL-88B(Fe) nanostructure, where the nanostructure exhibited a type III isotherm with a BET surface area of 4.9 $m^2\ g^{-1}$. This low surface area could be related to the breathing characteristic of the MIL-88B nanostructure, which is known to exhibit variable (low-to-high) surface area depending on reaction conditions.[39]

The effect of loading MIL-88B(Fe) with different percentages of Safranal on the structure and morphology of the formed SAF@MIL-88B(Fe) composite nanostructures is shown in Fig. 2–4. Fig. 2(a) shows the XRD patterns of the SAF@MIL-88B(Fe) nanostructures, where a consistent stability of the phase composition of the MIL-88B(Fe) structure was observed by increasing the concentration of SAF. All XRD peaks in the patterns of the SAF@MIL-88B(Fe) nanostructures were indexed with those shown in the XRD pattern of the pure MIL-88B(Fe). However, an additional peak was observed at 8.73° with increasing intensity upon increased SAF content. The presence of this peak could be related to the inclusion of the SAF molecule within the intrinsic porosity of the MIL-88B(Fe). The presence of Safranal in the SAF@MIL-88B(Fe) nanostructures was further confirmed by FTIR and TGA-DTG analyses. Fig. 2(b) shows the FTIR spectra of the SAF@MIL-88B(Fe) as compared with that of pure
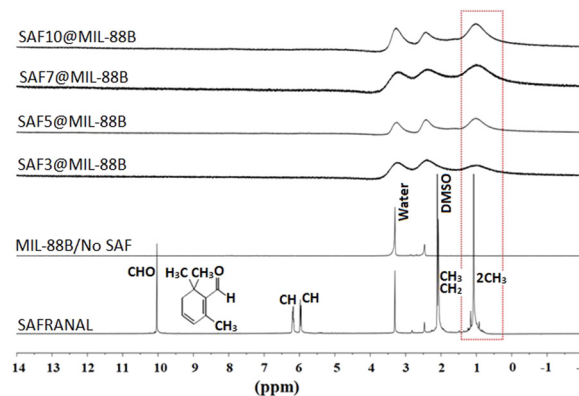

Fig. 3 ^{1}H NMR spectra of pure MIL-88B(Fe) and SAF@MIL-88 B(Fe) nanostructures containing 3, 5, 7, and 10% SAF as compared With that of pure SAF, demonstrating the continued existence of SAF within the MIL-88B(Fe) nanostructures.

MIL-88B(Fe). All spectra confirmed the structure MIL-88B(Fe). In addition, two low-intensity bands were observed at 2870 and 2968 cm^{-1}, and an additional band was observed at 679 cm^{-1}. These bands refer to the absorption of the C–H (of CH_3) and –C=O (of –CHO) of Safranal. These bands are identified in the FTIR spectrum of pure Safranal oil shown in Fig. S3 (ESI†).

Fig. 2(c) shows the TGA thermograms of the SAF@MIL-88B(Fe) composite nanostructures. Compared with the two main thermal events of the SAF-free MIL-88B(Fe), as shown in
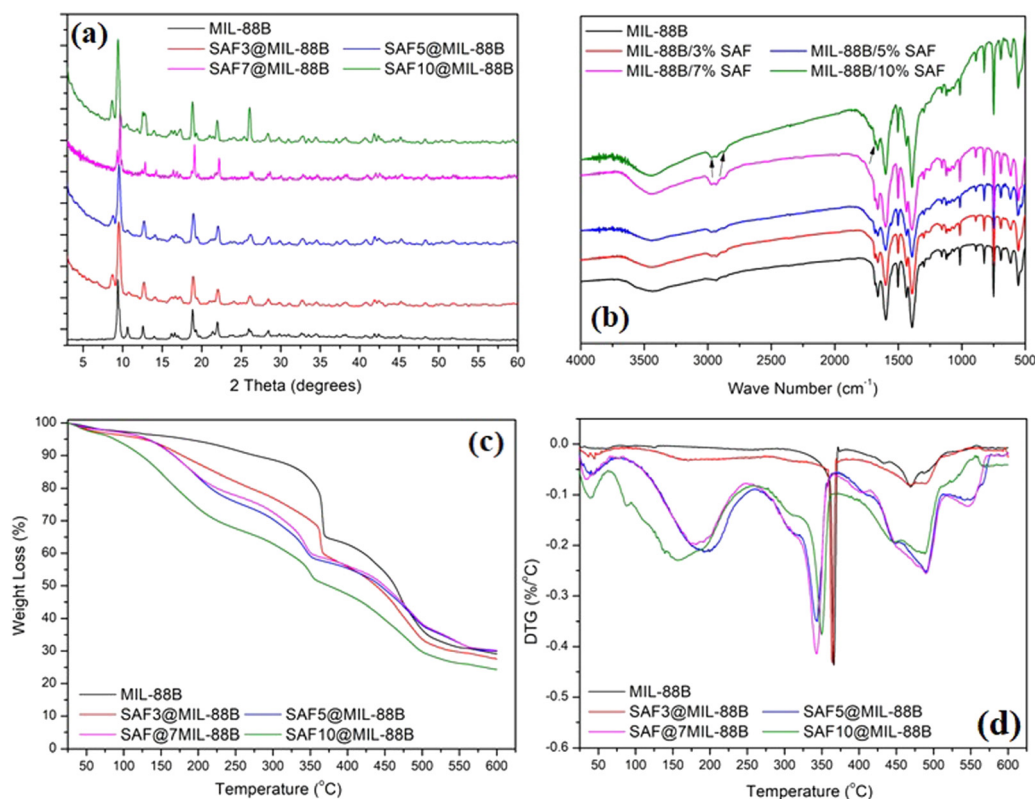

Fig. 2 XRD pattern (a), FT–IR spectra (b), TGA (c), and DTG (d) thermograms of pure MIL-88(Fe) and SAF@MIL-88(Fe) nanostructures containing 3, 5, 7, and 10% SAF. Arrows in Fig. 2(b) refer to the presence of safranal in the SAF@MIL-88 nanostructures.
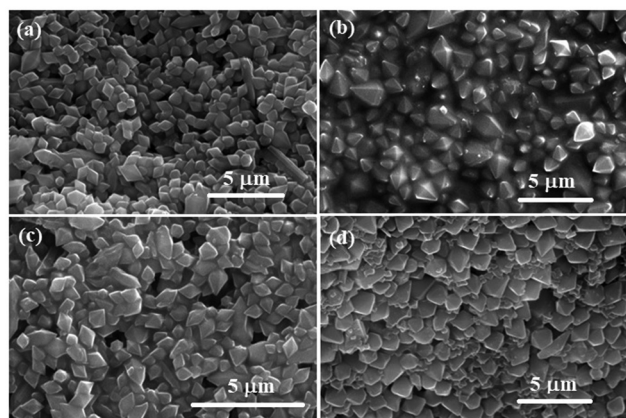
Fig. 4 SEM micrographs of SAF@MIL-88B(Fe) nanostructures containing (a) 3, (b) 5, (c) 7, and (d) 10% SAF.

Fig. 1(c), all TGA thermograms of the composite nanostructures showed multiple thermal events. This was further confirmed in the DTG thermograms of the composite nanostructures in Fig. 2(d). The multiple thermal events are summarized in Table 1. The first thermal event was observed in the range of 34–55 °C, and the second thermal event was observed in the range of 155–200 °C, both with increasing intensity with the increase of the safranal content. These events amount to an overall weight loss of 40%. These events could be related to the removal of the weakly adsorbed solvent and safranal molecules. These events were followed by a more shallow thermal event within the range of 349–367 °C with a shift towards lower temperature upon the increase of the safranal content. This event was followed by a more pronounced thermal event within the range of 432–470 °C with the same trend of increasing intensity upon increasing the safranal content. The third thermal event within the range of 349–367 °C could be attributed to the breakdown of the MOF structure, and the variation in the average temperature of its occurrence could be related to the presence of the more volatile, chemically bonded safranal molecules within the porosity of the MOF nanostructure. The fourth thermal event within the range of 432–470 °C could be attributed to the decomposition of the organic content of the nanostructures, and the increased intensities of these events with increasing the safranal content could be related to the presence of safranal-linker and/or safranal-coordinated Fe–O clusters within the structure. The last thermal event was observed within the range of 469–490 °C. It could be related to the decomposition of Safranal-coordinated Fe–O clusters, which is confirmed by its occurrence in the SAF@MIL-88B(Fe) thermograms and its absence in the thermogram of the pure MIL-88B(Fe) nanostructure.

It should be mentioned that the analysis of the aliquots produced, after suspending MIL-88B(Fe) in the SAF solutions containing 3, 5, 7, and 10% of SAF, using UV-vis confirmed the complete incorporation of SAF within the MIL-88B(Fe) structure. No signs of remaining SAF were observed in these aliquots. Based on the breathing effect of MIL-88B(Fe), it is known that MIL-88B(Fe) mostly adopts the closed structure while in the solid state, and opens up its porosity when in solution.[6,7] It is, therefore, believed that the incorporation of SAF in the MIL-88B(Fe) structure in solution takes place within the temporarily open porosity of the MIL-88B(Fe) when mixed in PBS media, as well as immobilized onto the external surfaces of the MIL-88B(Fe) structure through potential H-bonding formation. Fig. S4 (ESI†) shows a schematic representation of the interaction between a Safranal molecule within the pore and onto the surface of a MIL-88B(Fe) structure. Considering an average pore size of 62 nm of the open structure of MIL-88B(Fe) and an average size of 8 nm of a typical Safranal molecule, it is apparent that safranal molecules can be entrapped within the open pores of the MIL-88B(Fe) in solution in addition to adsorption on the external surfaces of the MIL-88B(Fe) nanostructure. The interaction between the Safranal molecules in both cases is believed to take place through H-bonding and coordination bonding formation, as indicated in Fig. S4 (ESI†).

The presence of Safranal within the nanostructure of the MIL-88B(Fe) was further confirmed by ^{1}H NMR, as shown in Fig. 3, as a function of the loading of Safranal in the nanostructure. The absence or poor appearance of hydrogen nuclear magnetic resonance (H-NMR) signals for SAF@MIL-88B(Fe) composite nanostructures can be attributed to many iron complexes being paramagnetic due to the presence of unpaired electrons in the d orbitals of the iron ion. On the other hand, the continued presence of a broad peak at a chemical shift of 1.2 ppm with increasing the safranal contents is an indication of the ^{1}H of the 2 CH$_3$ groups along the structure of the safranal molecule. The peak broadening observed in the spectra of the SAF@MIL-88B(Fe) composite nanostructures could be attributed to the paramagnetic characteristics of the iron complex structure. As a result, signals from individual protons become less resolved and may merge into a broad hump or baseline, making it challenging to assign peaks to their corresponding protons. Both DMSO and Water were shown as sharp peaks at 2.1 and 3.3 ppm, respectively. These peaks were also observed with more broadening in the NMR spectra of the SAF@MIL-88B(Fe) composite nanostructures.

To confirm the presence of the ^{1}H of the 2 CH$_3$ groups along the safranal molecule in the SAF@MIL-88B(Fe) as compared with the peaks of the solvents (DMOS and H$_2$O) used, a composite nanostructure containing the highest loading of safranal (10%) was titrated against deuterated HCl (DCl), as shown in Fig. S5 (ESI†). The peaks at 1.2 and 2.1 ppm, attributed to the ^{1}H of the safranal 2CH$_3$ groups and the DMSO solvent, were continuously present in the spectra of all samples upon increasing the volume of DCl. On the other hand, the peak at 3.3, which is attributed to ^{1}H of water, was observed to shift towards higher chemical shifts with increasing the volume

Table 1 Thermal events depicted from the TGA-DTG thermograms of MIL-88B(Fe) and SAF@MIL-88B(Fe) nanostructures

[SAF] (%)	Thermal events – peak temperatures				
0	53.6	None	366.3	432.5	469.5
3	45.1	176.3	364.1	469.0	488.4
5	45.1	194.5	342.9	448.4	489.6
7	34.8	179.7	342.9	448.4	489.6
10	39.9	156.9	349.7	448.4	489.6

of DCl. To further confirm this finding, a similar titration experiment was conducted for pure safranal, where the ^{1}H of water peak at 3.3 was shifted to higher chemical shifts with increasing the volume of DCl, as shown in Fig. S6 (ESI†). These findings further confirm the presence of safranal within the MIL-88B(Fe) nanostructure.

The effect of including safranal within the MIL-88B(Fe) nanostructure on the morphology of the produced crystals was examined using SEM microscopy, as shown in Fig. 4. The diamond-shape morphology of the MIL-88B(Fe) crystals was maintained with increasing the safranal loading. However, a slight deformation of the MIL-88B(Fe) crystals was observed, especially at higher safranal loadings. With reference to the XRD patterns of these samples (Fig. 2(a)), the phase composition and crystallinity of the MIL-88B(Fe) nanostructures were maintained despite the observed variations in the surfaces of these nanostructures.

Stability of MIL-88B(Fe) and SAF@MIL-88B(Fe) nanostructures in aqueous media

The effect of soaking both MIL-88B(Fe) and SAF@MIL-88B(Fe) containing 7 wt% safranal in aqueous media was investigated. Two media types were tested: a phosphate buffer (1X) and RPMI, both at pH 7.4 for up to 72 hours. Fig. 5 shows the XRD patterns of the treated samples, where the XRD patterns of

the non-treated MIL-88B(Fe) and SAF7@MIL-88B(Fe) are also shown for comparison. The XRD patterns of the pure MIL-88B(Fe) soaked in PBS media for up to 72 hours show a gradual degradation of the MOF structure. The most characteristic peaks of the MIL-88B(Fe) nanostructure disappeared after 72 hours of immersion of the MIL-88B(Fe) in PBS. Two sharp peaks were observed at 17.6 and 28.1°, which could be attributed to the formation of crystalline iron(III) phosphate,[41] while the broadness of the pattern between 2θ: 25–40 could be related to the formation of amorphous iron(III) phosphate.[41] The degradation of the MIL-88B(Fe) was also supported by the SEM investigation of the degradation products, as shown in Fig. 6(a)–(c), where a gradual deformation of the MIL-88B(Fe) nanostructures can be seen. In contrast, the presence of safranal within the MIL-88B(Fe) nanostructure seems to protect the MOF structure against the effect of the PBS media. The XRD patterns of the SAF7@MIL-88B(Fe) samples shown in Fig. 5(c) indicate the continued presence of the MIL-88B(Fe) crystalline structure with a slight decrease in the crystallinity of the SAF7@MIL-88B(Fe) sample. This was also confirmed in the SEM micrographs of these samples in Fig. 6(g)–(i), where a partial deformation of the SAF7@MIL-88B(Fe) crystals was observed.

The effect of treatment of both MIL-88B(Fe) and SAF7@MIL-88B(Fe) nanostructures with RPMI media was also reflected in their composition and morphology, as shown in Fig. 5 and 6.
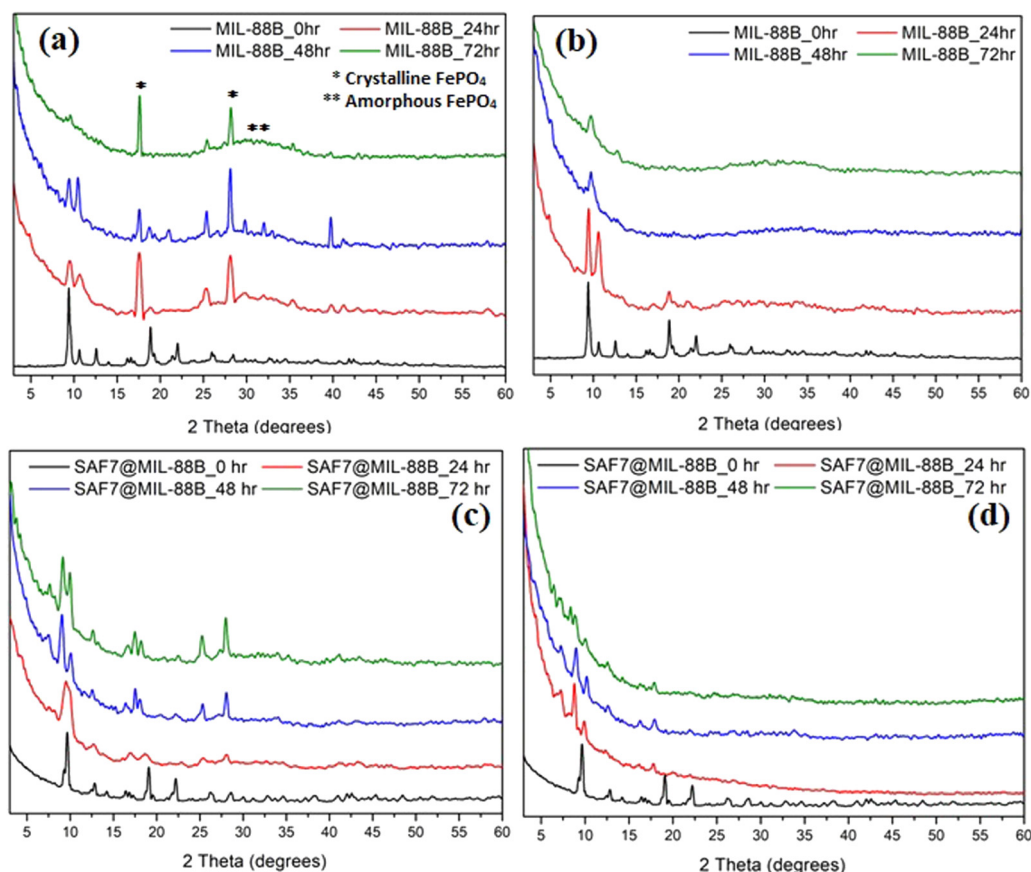

Fig. 5 XRD patterns of MIL–88B(Fe)(a), (b) and SAF7@MIL–88B(Fe) (c), (d) after incubation in PBS (a), (c) and RPMI (b), (d) media for 0, 24, 48 and 72 hours at 37 °C.
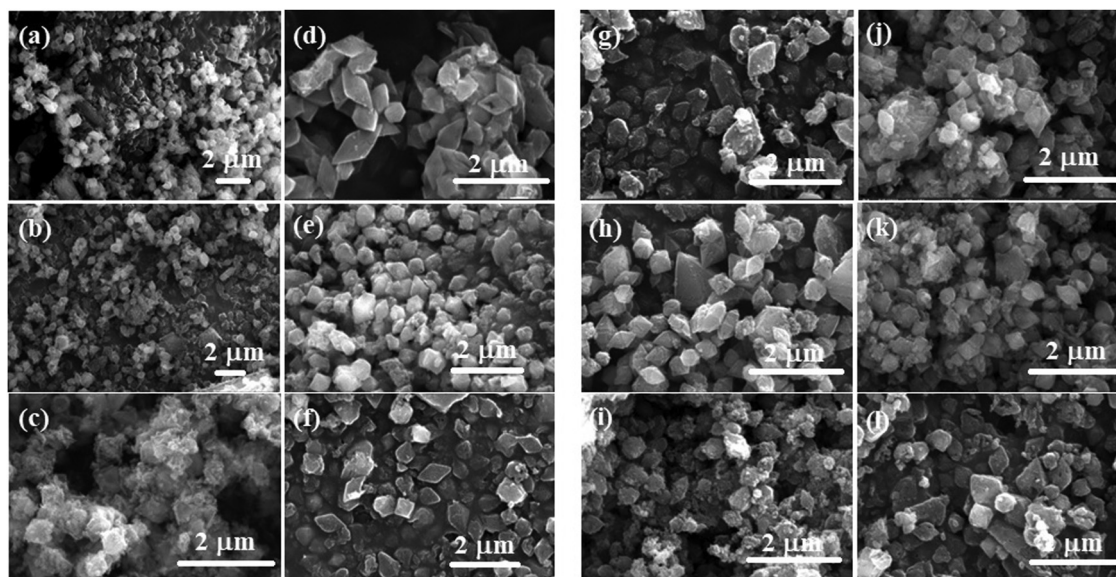
Fig. 6 SEM micrographs of MIL-88B(Fe) (a)–(f) and SAF7@MIL-88B(Fe) (g)–(l) after incubation in PBS (a)–(c) and (g)–(i) and RPMI (d)–(f) and (j)–(l) media for 24, 48 and 72 hours at 37 °C.

A gradual degradation of the MIL-88B(Fe) nanostructure in RPMI was also observed to take place with time, as shown in Fig. 5(b), which was also reflected in the morphology of the RPMI-treated MIL-88B(Fe) crystals (Fig. 6(d)–(f)). A similar pattern was observed for the SAF7@MIL-88B(Fe) crystals after immersion in RPMI media for up to 72 hours, where a gradual decrease in the crystallinity of the nanostructures was noticed (Fig. 5(d)). This was also accompanied by a visual decline in the sharpness of the SAF7@MIL-88B(Fe) crystals' morphology (Fig. 6(j)–(l)). The degradation of the MIL-88B and SAF7@-MIL-88B(Fe) nanostructures in PBS and RPMI media indicate their potential to degrade *in vitro*, hence releasing both Fe^{3+} ions and safranal with time *in vitro*.

The kinetics of release of Fe^{3+} ions and safranal from the MIL-88B(Fe) and SAF7@MIL-88B(Fe) nanostructures was monitored as a function of time. Fig. 7(a) shows a sudden release of Fe^{3+} ions from MIL-88B(Fe) and SAF7@MIL-88B(Fe) nanostructures within the first 60 minutes of immersion in PBS media.

The extent of release of Fe^{3+} ions was more pronounced in the case of SAF7@MIL-88B(Fe) than that of pure MIL-88B(Fe). Both nanostructures showed a decrease in the concentration of Fe^{3+} ions in solution within a course of 24 hours. The release of Fe^{3+} ions from the MIL-88B(Fe) and SAF7@MIL-88B(Fe) nanostructures ceased after 7 and 24 hours, respectively, followed by a minimal release throughout the experiment (up to 72 hours). These results agree with the XRD results shown in Fig. 5(a), where the formation of iron(III) phosphate was observed in the XRD pattern of the 24 hours-treated MIL-88B(Fe) sample. This indicates that the formation of the iron(III) phosphate structure is a product of the transformation of the MOF structure. The higher extent of release of Fe^{3+} ions from the SAF7@MIL-88B(Fe) indicates the possibility of chemical interaction between the safranal molecules and the Fe^{3+} clusters in the MIL-88B(Fe) MOF structure, which is confirmed by the release of safranal from the SAF7@MIL-88B(Fe) nanostructure within the same timeframe (Fig. 7(b)). The release of safranal from the SAF7@MIL-88B(Fe) nanostructure in Fig. 7(b)
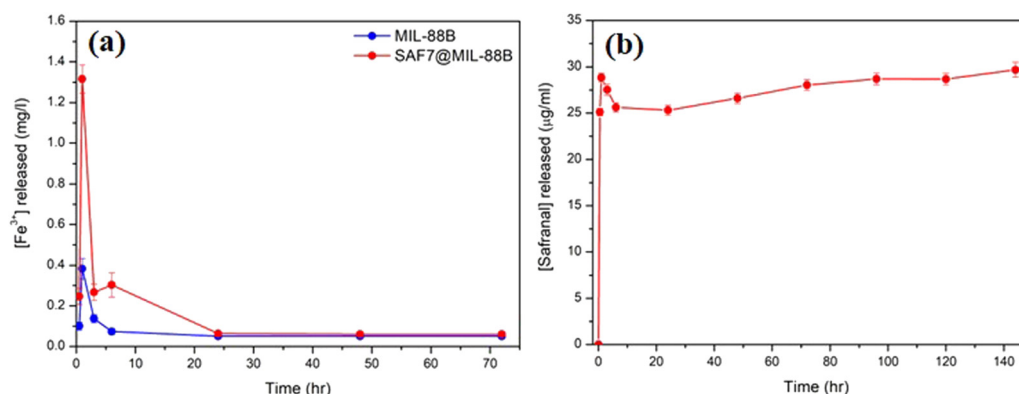

Fig. 7 (a) ICP analysis of the release of Fe^{3+} ions from pure MIL-88B(Fe) and SAF7@MIL-88B(Fe) after incubating in 1X PBS for up to 72 hours. (b) UV-VIS analysis of the release of Safranal from SAF7@MIL-88B(Fe) after incubating in 1× PBS for up to 144 hours.

shows a 2-phase release pattern. An initial burst is observed within the first 30 minutes (25.17 μg mL^{-1}) from SAF@MIL-88B(Fe), which is believed to be attributed to the detachment of the weakly adsorbed safranal molecules. This is followed by a second stage of sustained release of safranal reaching 28.0 μg mL^{-1} after 72 hours of immersion in PBS media.

It should be mentioned that safranal exhibits strong absorption in the 200–400 nm range with two distinct peaks at around 205 and 320 nm, attributed to the π–π* and n–π* transitions, respectively.[42] During the release study of safranal from the SAF7@MIL-88B(Fe) in PBS medium, the absorption at 205 nm only was observed, while the signal at 320 nm was absent (Fig. S1, ESI†). The absence of absorption at 320 nm, characteristic of safranal's n–π* transition, suggests that this particular molecular state or interaction was altered or disrupted. It is, therefore, considered a further confirmation of the interaction between the safranal molecule and MIL-88B(Fe) MOF structure, resulting in a change in the safranal's microenvironment leading to the disappearance of the n–π* transition at 320 nm.

The sustained release of safranal is likely attributed to the gradual diffusion of safranal molecules trapped within the MOF's porous structure. The pore size, surface properties, and interactions between MIL-88B(Fe) nanostructure and safranal molecules govern the diffusion rate, resulting in a controlled and prolonged release. This biphasic profile suggests potential advantages for using safranal therapeutically. The initial burst may have a faster therapeutic effect, which could be helpful for acute conditions that require prompt action. The sustained release ensures that safranal remains in the body for an extended time, potentially boosting overall therapy efficacy and reducing dose frequency, which can increase patient compliance. Furthermore, depending on the MOF design, the controlled release may allow the targeting of specific tissues or organs, reducing the possibility of side effects on healthy tissues.

Preliminary evaluation of the anti-cancer characteristics of MIL-88B(Fe) and SAF@MIL-88B(Fe) nanostructures

Studies have shown that safranal holds a promising effect on HepG2 cells. However, there is a scarcity of research that focuses on both the intrinsic features of MIL-88B(Fe) nanostructures and their drug-loading capabilities in relation to liver cancer cells. Limited research has been conducted in this area, emphasizing the need for more investigation to understand better the precise mechanisms of MIL-88B(Fe) in targeting liver cancer, and its potential as a drug delivery system for liver cancer therapy. Although safranal shows promising anticancer properties against HepG2 cells, its efficacy as a standalone anticancer agent could be limited for several reasons. Including its limited bioavailability, the specificity of safranal's anticancer effect may differ between different types of liver cancer cells, safranal's anticancer effects are dose-dependent, and prolonged safranal treatment may create resistance mechanisms within cancer cells, presenting a challenge to its long-term efficacy.

In this regard, pure MIL-88B(Fe) and that loaded with 7% safranal (SAF7@MIL-88B(Fe)) were evaluated for their cytotoxic effects against HepG2 liver cancer cells following 24 and 48-hour incubation periods. Fig. 8 and 9 depict the trend in cell viability of MIL-88B(Fe) and SAF7@MIL-88B(Fe), respectively, after 24 and 48 hours of incubation at 37 °C. Results indicate that both materials exhibit a dose-dependent effect on HepG2 cells. After 24 hours of incubation, MIL-88B(Fe) inhibited 50% of cells at 11.770 μg mL^{-1} (Fig. 8(a)), while SAF@MIL-88B(Fe) inhibited 50% of cells at 9.510 μg mL^{-1} (Fig. 9(a)). After 48 hours of exposure, cell viability reduced significantly, with IC$_{50}$s of 6.372 μg mL^{-1} (Fig. 8(b)) and 3.459 μg mL^{-1} (Fig. 9(b)) for MIL-88B(Fe) and SAF@MIL-88B(Fe), respectively. These findings indicate that both materials considerably influence the metabolic activity of HepG2 cells. Moreover, the values suggest a potential synergistic effect of MIL-88B(Fe) and safranal.

Nuclear morphology evaluation was carried out using DAPI staining, where DAPI (4′,6-diamidino-2-phenylindole) is a fluorescent dye that binds particularly to adenine–thymine (AT)-rich DNA segments, allowing cell nuclei to be visualized.[43] Following DAPI staining and fluorescence microscopy imaging, shown in Fig. 8(c) and 9(c), the observed nuclear morphology supports that MIL-88B(Fe) and SAF@MIL-88B(Fe) support the assumption of a dose-dependent effect on the treated cells. As the MOF concentration increased, apparent alterations in nuclear morphology were observed, including variations in size, shape, and intensity.

The dose-dependent pattern is more visible when the MOF concentration increases from lower to higher levels. Normal nuclei with uniform DAPI staining at lower doses were more prevalent; however, there was an apparent rise in condensed or fragmented nuclei at higher concentrations, indicating a potential trigger for cellular stress or apoptotic processes. These findings suggest narrowing the dose selection to 2.5–25 μg mL^{-1} for further investigation of the MOFs' impact on HepG2 cells. Future studies will utilize cellular assays and molecular analysis to investigate the mechanisms underlying this dose-dependent response.

Preliminary evaluation of the anti-bacterial characteristics of MIL-88B(Fe) and SAF@MIL-88B(Fe) nanostructures

Both MIL-88B(Fe) and SAF@MIL-88B(Fe) containing 7% safranal were evaluated for their antibacterial characteristics against *E. coli* and *Lactobacillus* strains. Fig. 10(a) and (b) shows the zone of inhibition of both strains using the MIL-88B(Fe) and SAF@-MIL-88B(Fe) nanostructures. The presence of MIL-88B(Fe) demonstrated significant antibacterial effects with 7 mm and 9.67 mm inhibition zone values on *E. coli* and *Lactobacillus*, respectively. On the other hand, SAF@MIL-88B(Fe) showed slightly lower inhibition zone areas with a 6.33 mm and 8.67 mm effect on *E. coli* and *Lactobacillus*, respectively. The release of iron from MIL-88B(Fe) and SAF@MIL-88B(Fe) within the inhibition zone area of *E. coli* has been investigated using the ICP-AES approach. The analysis revealed a considerably higher iron release from MIL-88B(Fe) at 1.89 mg mL^{-1}, whereas SAF@-MIL-88B(Fe) demonstrated a significantly lower value, falling below the detection limit (<0.05 mg mL^{-1}). The disparity shows that the strong bonding of safranal to the MOF structure slows the degradation process, which explains the observed difference
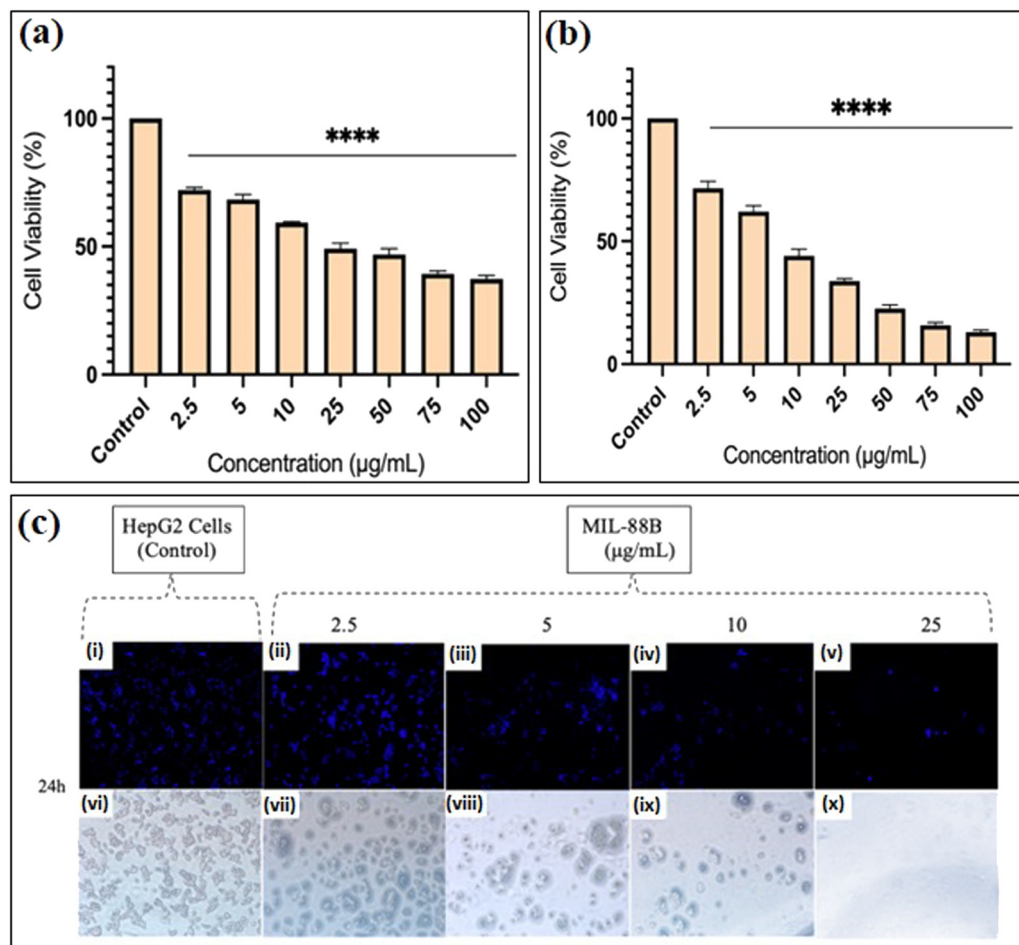
Fig. 8 Cell viability assay demonstrating the effects of incubation of MIL-88B(Fe) with HepG2 cancer cells for (a) 24 and (b) 48 hours at 37 °C. Statistical significance is denoted by $*P \leq 0.05$, $**P \leq 0.01$, $***P \leq 0.001$, and $****P \leq 0.00001$. (c) Fluorescent (i)–(v) and bright field (vi)–(x) microscopic images of hepatic cancer cells (HepG2) after 24 hours of incubation with (i) and (vi) received 0 mg mL^{-1} MIL-88B(Fe), (ii) and (vii) received 2.5 mg mL^{-1}, (iii) and (viii) received 5 mg mL^{-1}, (iv) and (ix) received 10 mg mL^{-1}, (v) and (x) received 25 mg mL^{-1} of MIL-88B(Fe) powder at 37 °C. Scale bar = 20 mm.

in inhibition zone values between MIL-88B(Fe) and SAF@MIL-88B(Fe). The slower release mechanism of SAF@MIL-88B(Fe) could be beneficial for achieving sustained and prolonged antibacterial action over time. Fig. S7 (ESI†) shows the antibacterial activity of the pure linker (terephthalic acid, TA) on both types of strains. Results show that TA does not affect *E. coli*. In contrast, TA exhibited a low inhibitory effect on *Lactobacillus*, as demonstrated by a 2 mm inhibition zone. The contribution of TA to the inhibition process is therefore believed to be minimal.

The minimum inhibitory concentration (MIC) for MIL-88B(Fe) and SAF@MIL-88B(Fe) nanostructures against *E. coli* and *Lactobacillus* at various concentrations (7.81–2000 µg) was carried out, as shown in Fig. S8 and S9 (ESI†). Following a 16-hour treatment period, both MOF nanostructures had inhibitory effects against bacterial strains at the maximum concentration tested at 2000 µg (Tables S1 and S2, ESI†). Furthermore, MIL-88B(Fe) and SAF@MIL-88B(Fe) displayed partial inhibition at a concentration of 1000 µg. These results show the antibacterial activity of both Fe-MOFs against *E. coli* and *Lactobacillus*, with the same levels of inhibition observed at different concentrations.

The mechanism of antimicrobial activity of both types of MOF nanostructures was analyzed by the DNA disintegration method, which indicates the inhibition of nucleic acid synthesis while incubating microorganisms in the presence of MOFs, as shown in Fig. 10(c)–(f). MIL-88B(Fe) achieved total degradation on *E. coli* as observed in lanes 3, 4, and 5 (0.5, 1, and 1.5 times the MIC) (Fig. 10(c)). The spectrum of the impact caused by SAF@MIL-88B(Fe) on *E. coli* is shown in Fig. 10(d), with partial degradation observed in lanes 1–3 (0.125, 0.25, and 0.5 times the MIC) and total degradation in lanes 4 and 5 (1 and 1.5 times the MIC). Results are also summarized in Tables S3 and S4 (ESI†) using a Nanodrop 2000 (Thermo Fisher). The data shown in Table S3 (ESI†) show a decrease in DNA concentration as the concentration of MIL-88B(Fe) increased. This is consistent with the observation that MIL-88B(Fe) effectively degrades *E. coli* DNA. Furthermore, Table S4 (ESI†) presents the DNA quantification of *E. coli* treated with SAF@MIL-88B(Fe). Similar to MIL-88B(Fe), SAF@MIL-88B(Fe) demonstrates a dose-dependent effect on DNA degradation. As the SAF@MIL-88B(Fe) concentration increased, the DNA concentration progressively decreased. This observation aligns with the findings from Fig. 10(c) and (d), which visually
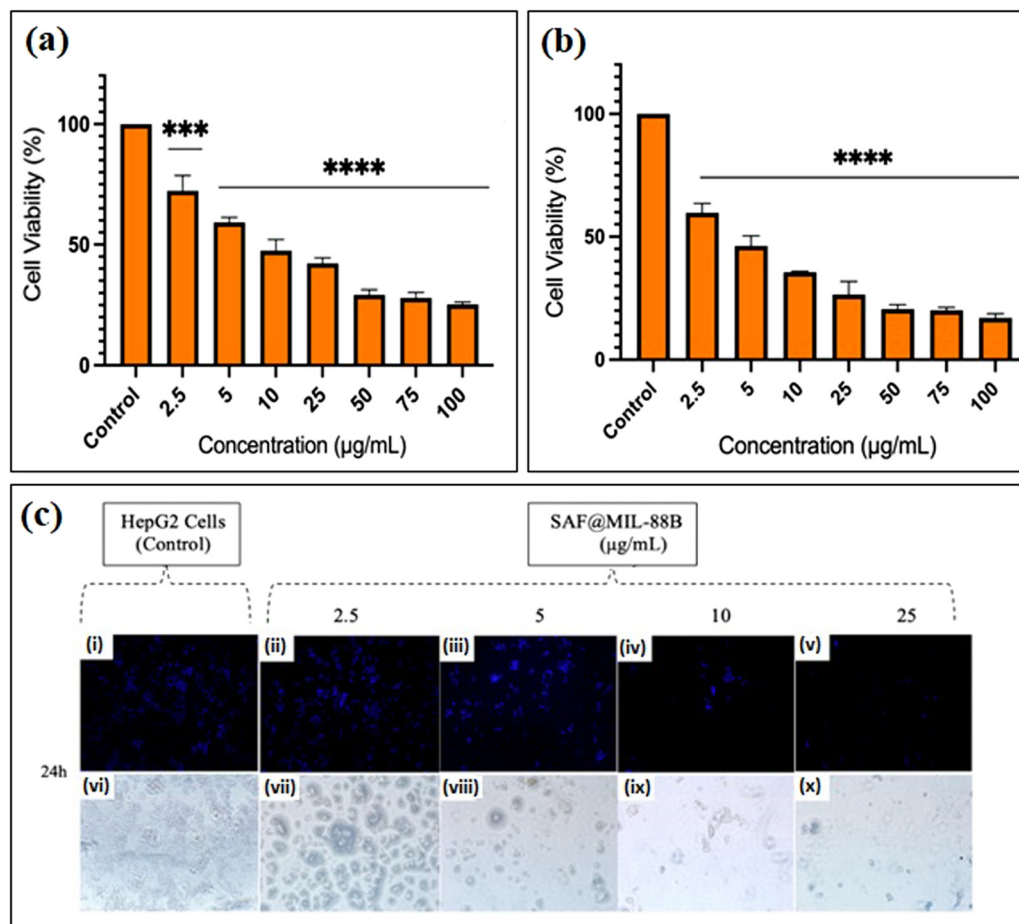
Fig. 9 Cell viability assay demonstrating the effects of incubation of SAF@MIL-88B(Fe) with HepG2 cancer cells for (a) 24 and (b) 48 hours at 37 °C. Statistical significance is denoted by $*P \leq 0.05$, $**P \leq 0.01$, $***P \leq 0.001$, and $****P \leq 0.00001$. (c) Fluorescent (i)–(v) and bright field (vi)–(x) microscopic images of hepatic cancer cells (HepG2) after 24 hours of incubation with (i) and (vi) received 0 mg mL^{-1} SAF@MIL-88B(Fe), (ii) and (vii) received 2.5 mg mL^{-1}, (iii) and (viii) received 5 mg mL^{-1}, (iv) and (ix) received 10 mg mL^{-1}, (v) and (x) received 25 mg mL^{-1} of MIL-88B(Fe) powder at 37 °C. Scale bar = 20.
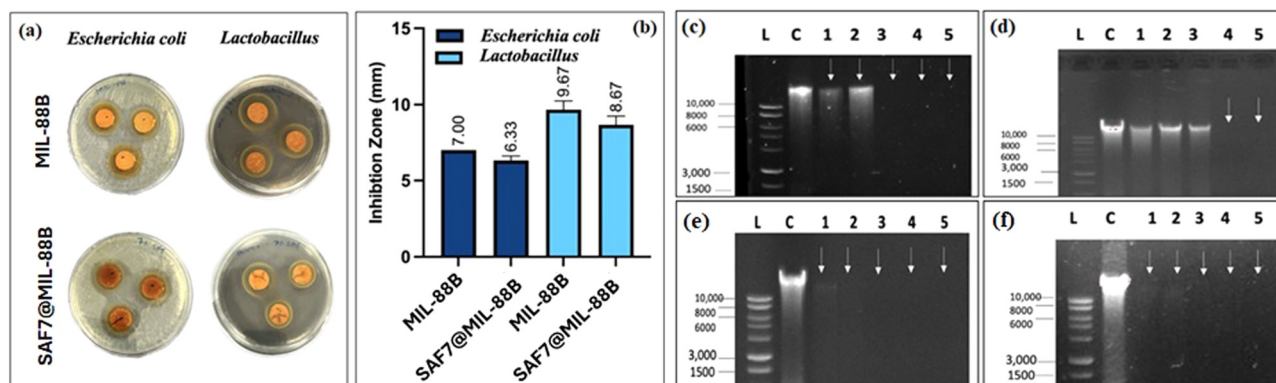

Fig. 10 (a) Antibacterial activity of MIL-88B(Fe) and SAF7@MIL88B(Fe) against *E. coli* and *Lactobacillus* and their respective zone of inhibition (b). DNA agarose electrophoresis of *E. coli* (c), (d) and *Lactobacillus* (e), (f) treated with various concentrations of MIL-88B(Fe) (c), (e) and SAF@MIL-88B(Fe) (d), (f) particles. L: kb DNA ladder (Promega), C:control of each bacterial strain without treatment, 1: 0.125 × MIC, 2: 0.25 × MIC, 3: 0.5 × MIC, 4: 1 × MIC, and 5: 1.5 × MIC.

depicted partial degradation at lower concentrations and complete degradation at higher concentrations of both MOF nanostructures.

The agarose gel electrophoresis of both MIL-88B(Fe) and SAF@MIL-88B(Fe) caused complete degradation of *Lactobacillus* DNA across a concentration range ranging from 0.125 to
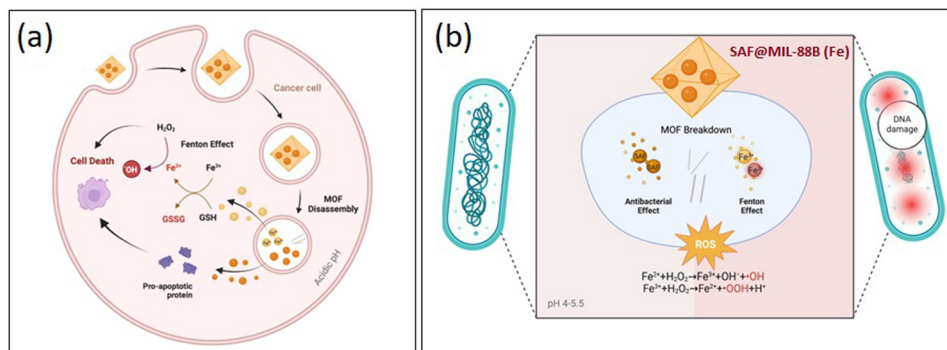
Scheme 2 Mechanism of action showing the anticancer (a) and antibacterial (b) capabilities of the SAF@MIL-88B(Fe) nanostructures.

1.5 times the MIC. Fig. 10(e) and (f) visually demonstrate this genotoxic effect, respectively. Table S5 (ESI†) explores *Lactobacillus* treated with MIL-88B(Fe) and indicates a dose-dependent decline in DNA concentration. All concentrations tested showed a significant and notable reduction in DNA concentration, aligning with the complete degradation observed in Fig. 10(e). Table S6 (ESI†) examines *Lactobacillus* treated with SAF@MIL-88B(Fe), also displaying a dose-dependent decrease in DNA concentration, aligning with the complete degradation observed in Fig. 10(f). These DNA quantification tables provide quantitative evidence supporting the visual observations from the figures, solidifying the conclusion that both MIL-88B(Fe) and SAF@MIL-88B(Fe) MOF nanostructures are effective antibacterial agents against *E. coli* with a pronounced efficacy against *Lactobacillus*.

Proposed mechanism of anti-cancer and anti-bacterial characteristics of MIL-88B(Fe) and SAF@MIL-88B(Fe) nanostructures

MIL-88B(Fe) nanoparticles encapsulating safranal, as shown in Scheme 2, demonstrate dual activity against liver cancer cells and bacteria. MIL-88B(Fe) initially releases Fe^{3+} ions in the acidic tumor microenvironment, which are subsequently reduced to Fe^{2+} ions.

These Fe^{2+} ions participate in Fenton-like reactions with hydrogen peroxide, generating highly reactive hydroxyl radicals that can induce lipid peroxidation and oxidative stress, ultimately leading to ferroptosis—a specific form of cell death in cancer cells. Simultaneously, safranal within MIL-88B(Fe) contributes to the inhibition of cell proliferation of HepG2 cells, enhancing the cytotoxic effect of the nanoparticles. This action of MIL-88B(Fe) and safranal presents a potential strategy for targeted liver cancer therapy. On the antibacterial front, MIL-88B(Fe) nanoparticles release Fe^{2+} ions in the bacterial environment. These ions, along with safranal, can disrupt bacterial cell membranes, leading to damage to cellular components and DNA, ultimately resulting in bacterial death. This highlights the importance of future research to validate the proposed mechanism of action and optimize the therapeutic potential of MIL-88B(Fe) loaded with safranal against both liver cancer and bacterial infections.

Conclusions

In this study, we developed an iron-based metal–organic framework, MIL-88B(Fe), incorporating safranal, demonstrating its dual functionality against cancer and bacteria. Characterization techniques confirmed the successful synthesis of MIL-88B(Fe) and the effective loading of safranal. The synthesized nanomaterials exhibited inhibition of HepG2 liver cancer cells and showed antibacterial effects against *Escherichia coli* and *Lactobacillus* strains, presenting avenues for innovative multifunctional materials in biotechnology. Further *in vitro* studies are needed to understand the mechanisms of these materials against HepG2 cells comprehensively. Moreover, the findings provide compelling evidence for the antibacterial efficacy of MIL-88B(Fe) and SAF@MIL-88B(Fe) against *E. coli*, with a notably more substantial effect observed on Lactobacillus. The inhibition zone assay revealed significant bacterial growth inhibition, while the minimum inhibitory concentration (MIC) assay demonstrated partial inhibition at 1000 μg and complete inhibition at 2000 μg. Future experiments will focus on the 1000 μg to 2000 μg range for more precise results. Acknowledging the experimental limitations, confined to a 16-hour incubation period, future investigations will extend incubation to 24 and 48 hours to better understand the MOFs' antimicrobial activity over prolonged durations. DNA quantification and disintegration assays also highlighted the genotoxic effects of these MOFs, further supporting their potential as effective antibacterial agents. Further analysis and experimentation will contribute to a deeper understanding of the mechanisms underlying the antibacterial activity of MIL-88B(Fe) and SAF@MIL-88B(Fe).

Data availability

This is to confirm that the data presented in this manuscript have been already included in the main file of the manuscript as well as the supplementary section. No animal study results or other data are available anywhere else or claimed at any other site.

Conflicts of interest

There are no conflicts to declare.

Acknowledgements

References

1 R. Freund; S. Canossa; S. M. Cohen; W. Yan; H. Deng; V. Guillerm; M. Eddaoudi; D. G. Madden; D. Fairen-Jimenez; H. Lyu; L. K. Macreadie; Z. Ji; Y. Zhang; B. Wang; F. Haase; C. Wöll; O. Zaremba; J. Andreo; S. Wuttke and C. S. Diercks, 25 Years of Reticular Chemistry. n/a (n/a).

2 R. Freund; O. Zaremba; G. Arnauts; R. Ameloot; G. Skorupskii; M. Dincă; A. Bavykina; J. Gascon; A. Ejsmont; J. Gościańska; M. Kalmutzki; U. Lächelt; E. Ploetz; C. Diercks and S. Wuttke, The Current Status of MOF and COF Applications. n/a (n/a).

3 R. Freund, U. Lächelt, T. Gruber, B. Rühle and S. Wuttke, Multifunctional Efficiency: Extending the Concept of Atom Economy to Functional Nanomaterials, *ACS Nano*, 2018, **12**(3), 2094–2105.

4 K. Leus; I. Muylaert; V. Van Speybroeck; G. B. Marin and P. Van Der Voort, A coordinative saturated vanadium containing metal organic framework that shows a remarkable catalytic activity, in *Studies in Surface Science and Catalysis*, ed. E. M. Gaigneaux, M. Devillers, S. Hermans, P. A. Jacobs, J. A. Martens and P. Ruiz, Elsevier: 2010, vol. 175, pp.329–332.

5 J. L. C. Rowsell and O. M. Yaghi, Metal–organic frameworks: a new class of porous materials, *Microporous Mesoporous Mater.*, 2004, **73**(1), 3–14.

6 M. Ma, A. Bétard, I. Weber, N. S. Al-Hokbany, R. A. Fischer and N. Metzler-Nolte, Iron-based metal–organic frameworks MIL-88B and NH2- MIL-88B: high quality microwave synthesis and solvent-induced lattice "breathing", *Cryst. Growth Des.*, 2013, **13**, 2286e91.

7 C. Mellot-Draznieks, C. Serre, S. Surble, N. Audebrand and G. Férey, Very large swelling in hybrid frameworks: a combined computational and powder diffraction study, *J. Am. Chem. Soc.*, 2005, **127**, 12273e85.

8 P. Horcajada, C. Serre, G. Maurin, N. A. Ramsahye, F. Balas and M. Vallet-Regí, *et al.*, Flexible porous metal–organic frameworks for a controlled drug delivery, *J. Am. Chem. Soc.*, 2008, **130**, 6774e80.

9 S. R. Miller, D. Heurtaux, T. Baati, P. Horcajada, J.-M. Grenèche and C. Serre, Biodegradable Therapeutic MOFs for the Delivery of Bioactive Molecules, *Chem. Commun.*, 2010, **46**, 4526–4528.

10 S. Keskin and S. Kızılel, Biomedical Applications of Metal organic Frameworks, *Ind. Eng. Chem. Res.*, 2011, **50**, 1799–1812.

11 M. Al Haydar, H. Abid, B. Sunderland and S. Wang, Metal organic Frameworks as a Drug Delivery System for Flurbiprofen, *Drug Des., Dev. Ther.*, 2017, **11**, 2685–2695.

12 P. Horcajada, C. Serre, G. Maurin, N. A. Ramsahye, F. Balas, M. Vallet-Regí, M. Sebban, F. Taulelle and G. Férey, Flexible Porous Metal-organic Frameworks for a Controlled Drug Delivery, *J. Am. Chem. Soc.*, 2008, **130**, 6774–6780.

13 M. Giménez-Marqués, T. Hidalgo, C. Serre and P. Horcajada, Nanostructured Metal–organic Frameworks and Their Bio-Related Applications, *Coord. Chem. Rev.*, 2016, **307**, 342–360.

14 P. Horcajada, F. Salles, S. Wuttke, T. Devic, D. Heurtaux, G. Maurin, A. Vimont, M. Daturi, O. David and E. Magnier, *et al.*, How Linker's Modification Controls Swelling Properties of Highly Flexible Iron(III) Dicarboxylates MIL-88, *J. Am. Chem. Soc.*, 2011, **133**, 17839–17847.

15 C. Serre, S. Surblé, C. Mellot-Draznieks, Y. Filinchuk and G. Férey, Evidence of Flexibility in the Nanoporous Iron(III) Carboxylate MIL-89, *Dalton Trans.*, 2008, 5462.

16 S. Surblé, C. Serre, C. Mellot-Draznieks, F. Millange and G. Férey, A New Isoreticular Class of Metal-organic-Frameworks with the MIL-88 Topology, *Chem. Commun.*, 2006, 284–286.

17 A. C. McKinlay, R. E. Morris, P. Horcajada, G. Férey, R. Gref, P. Couvreur and C. Serre, BioMOFs: Metal–organic Frameworks for Biological and Medical Applications, *Angew. Chem., Int. Ed.*, 2010, **49**, 6260–6266.

18 T. Baati, L. Njim, F. Neffati, A. Kerkeni, M. Bouttemi, R. Gref, M. F. Najjar, A. Zakhama, P. Couvreur, C. Serre and P. Horcajada, *Chem. Sci.*, 2013, **4**, 1597–1607, DOI: 10.1039/c3sc22116d.

19 C. Tamames-Tabar, D. Cunha, E. Imbuluzqueta, F. Ragon, C. Serre, M. J. Blanco-Prieto and P. Horcajada, *J. Mater. Chem. B*, 2014, **2**, 262–271, DOI: 10.1039/c3tb20832j.

20 S. Rojas, T. Baati, L. Njim, L. Manchego, F. Neffati, N. Abdeljelil, S. Saguem, C. Serre, M. F. Najjar, A. Zakhama and P. Horcajada, *J. Am. Chem. Soc.*, 2018, **140**, 9581–9586, DOI: 10.1021/jacs.8b04435.

21 P. Horcajada, T. Chalati, C. Serre, B. Gillet, C. Sebrie, T. Baati, J. F. Eubank, D. Heurtaux, P. Clayette, C. Kreuz, J. S. Chang, Y. K. Hwang, V. Marsaud, P. N. Bories, L. Cynober, S. Gil, G. Férey, P. Couvreur and R. Gref, Porous metal-organic-framework nanoscale carriers as a potential platform for drug delivery and imaging, *Nat. Mater.*, 2010, **9**(2), 172–178, DOI: 10.1038/NMAT2608.

22 C. Tamames-Tabar, D. Cunha, E. Imbuluzqueta, F. Ragon, C. Serre, M. J. Blanco-Prieto and P. Horcajada, Cytotoxicity of nanoscaled metal–organic frameworks, *J. Mater. Chem. B*, 2013, **2**(3), 262–271, DOI: 10.1039/C3TB20832J.

23 J. Joseph, S. Iftekhar, V. Srivastava, Z. Fallah, E. N. Zare and M. Sillanpää, Iron-based metal-organic framework: Synthesis, structure and current technologies for water reclamation with deep insight into framework integrity, *Chemosphere*, 2021, **284**, 131171, DOI: 10.1016/J.CHEMOSPHERE.2021.131171.

24 B. Thakur, V. v Karve, D. T. Sun, A. L. Semrau, L. J. K. Weiß, L. Grob, R. A. Fischer, W. L. Queen and B. Wolfrum, An Investigation into the Intrinsic Peroxidase-Like Activity of Fe-MOFs and Fe-MOFs/Polymer Composites, *Adv. Mater. Technol.*, 2021, **6**(5), 2001048, DOI: 10.1002/ADMT.202001048.

25 X. N. Wang, Y. Zhao, J. L. Li, J. D. Pang, Q. Wang, B. Li and H. C. Zhou, Biomimetic catalysts of iron-based metal–organic frameworks with high peroxidase-mimicking activity for colorimetric biosensing, *Dalton Trans.*, 2021, **50**(11), 3854–3861, DOI: 10.1039/D0DT02504F.

26 S. M. Sheta, S. R. Salem and S. M. El-Sheikh, A novel Iron(III)-based MOF: Synthesis, characterization, biological, and

antimicrobial activity study, *J. Mater. Res.*, 2022, **37**(14), 2356–2367, DOI: **10.1557/S43578-022-00644-9/SCHEMES/1**.

27 R. Zhu, M. Cai, T. Fu, D. Yin, H. Peng, S. Liao, Y. Du, J. Kong, J. Ni and X. Yin, Fe-Based Metal Organic Frameworks (Fe-MOFs) for Bio-Related Applications, *Pharmaceutics*, 2023, **15**(6), 1599, DOI: **10.3390/PHARMACEUTICS15061599**.

28 X. Wan, L. Song, W. Pan, H. Zhong, N. Li and B. Tang, Tumor-Targeted Cascade Nanoreactor Based on Metal-Organic Frameworks for Synergistic Ferroptosis-Starvation Anticancer Therapy, *ACS Nano*, 2020, **14**(9), 11017–11028, DOI: **10.1021/ACSNANO.9B07789/SUPPL_FILE/NN9B07789_SI_001.PDF**.

29 S. Wang, H. Wu, K. Sun, J. Hu, F. Chen, W. Liu, J. Chen, B. Sun and A. M. S. Hossain, A novel pH-responsive Fe-MOF system for enhanced cancer treatment mediated by the Fenton reaction, *New J. Chem.*, 2021, **45**(6), 3271–3279, DOI: **10.1039/D0NJ05105E**.

30 J. Yang, S. Ma, R. Xu, Y. Wei, J. Zhang, T. Zuo, Z. Wang, H. Deng, N. Yang and Q. Shen, Smart biomimetic metal organic frameworks based on ROS-ferroptosis-glycolysis regulation for enhanced tumor chemo-immunotherapy, *J. Controlled Release*, 2021, **334**, 21–33.

31 M. U. Akbar, A. Akbar, U. A. K. Saddozai, M. I. U. Khan, M. Zaheer and M. Badar, A multivariate metal–organic framework based pH-responsive dual-drug delivery system for chemotherapy and chemodynamic therapy, *Mater. Adv.*, 2023, **4**(22), 5653–5667, DOI: **10.1039/D3MA00389B**.

32 A. Al-Hrout, A. Chaiboonchoe, B. Khraiwesh, C. Murali, B. Baig, R. El-Awady, H. Tarazi, A. Alzahmi, D. R. Nelson, Y. E. Greish, W. Ramadan, K. Salehi-Ashtiani and A. Amin, Safranal induces DNA double-strand breakage and ER-stress-mediated cell death in hepatocellular carcinoma cells, *Sci. Rep.*, 2018, **8**(1), 1–15, DOI: **10.1038/s41598-018-34855-0**.

33 A. Abdalla, C. Murali and A. Amin, Safranal Inhibits Angiogenesis via Targeting HIF-1α/VEGF Machinery: *In Vitro* and *Ex Vivo* Insights, *Front. Oncol.*, 2022, **11**, 789172, DOI: **10.3389/FONC.2021.789172/BIBTEX**.

34 A. Dogra, P. Kotwal, A. Gour, S. Bhatt, G. Singh, D. Mukherjee and U. Nandi, Description of Druglike Properties of Safranal and Its Chemistry behind Low Oral Exposure, *ACS Omega*, 2020, **5**(17), 9885–9891, DOI: **10.1021/acsomega.0c00160**.

35 J. Liu, D. Wu, N. Zhu, Y. Wu and G. Li, Antibacterial mechanisms and applications of metal-organic frameworks and their derived nanomaterials, *Trends Food Sci. Technol.*, 2021, **109**, 413–434, DOI: **10.1016/J.TIFS.2021.01.012**.

36 L. Wang, C. Hu and L. Shao, The antimicrobial activity of nanoparticles: present situation and prospects for the future, *Int. J. Nanomed.*, 2017, **12**, 1227, DOI: **10.2147/IJN.S121956**.

37 X. Zhang, F. Peng and D. Wang, MOFs and MOF-Derived Materials for Antibacterial Application, *J. Funct. Biomater.*, 2022, **13**(4), 215, DOI: **10.3390/JFB13040215**.

38 S. Hou, Y. Wu, L. Feng, W. Chen, Y. Wang, C. Morlay and F. Li, Green synthesis and evaluation of an iron-based metal-organic framework MIL-88B for efficient decontamination of arsenate from water, *Dalton Trans.*, 2018, **47**, 2222, DOI: **10.1039/c7dt03775a**.

39 S. Hou, Y. N. Wu, L. Feng, W. Chen, Y. Wang, C. Morlay and F. Li, Green synthesis and evaluation of an iron-based metal–organic framework MIL-88B for efficient decontamination of arsenate from water, *Dalton Trans.*, 2018, **47**(7), 2222–2231, DOI: **10.1039/C7DT03775A**.

40 M. Y. Zorainy, S. Kaliaguine, M. Gobara, S. Elbasuney and D. C. Boffito, Microwave-Assisted Synthesis of the Flexible Iron-based MIL-88B Metal–Organic Framework for Advanced Energetic Systems, *J. Inorg. Organomet. Polym. Mater.*, 2022, **32**(7), 2538–2556, DOI: **10.1007/S10904-022-02353-6/METRICS**.

41 D. Jiang, X. Zhang, T. Zhao, B. Liu, R. Yang, H. Zhang, T. Fan and F. Wang, An improved synthesis of iron phosphate as a precursor to synthesize lithium iron phosphate, *Bull. Mater. Sci.*, 2020, **43**(1), 1–7, DOI: **10.1007/S12034-019-1994-Y/METRICS**.

42 M. S. Ali and H. A. Al-Lohedan, Spectroscopic and Molecular Docking Investigation on the Noncovalent Interaction of Lysozyme with Saffron Constituent "Safranal, *ACS Omega*, 2020, **5**(16), 9131–9141, DOI: **10.1021/ACSOMEGA.9B04291**.

43 R. Huschka, O. Neumann, A. Barhoumi and N. J. Halas, Visualizing light-triggered release of molecules inside living cells, *Nano Lett.*, 2010, **10**(10), 4117, DOI: **10.1021/NL102293B**.